

# A Segmented, Enriched N-type Germanium Detector for Neutrinoless Double Beta-Decay Experiments

L. E. Leviner<sup>a,b</sup>, C. E. Aalseth<sup>e</sup>, M. W. Ahmed<sup>c,b</sup>, F. T. Avignone III<sup>e,i</sup>, H. O. Back<sup>a,b,q</sup>, A. S. Barabash<sup>m</sup>, M. Boswell<sup>f</sup>, L. De Braekeleer<sup>b,c</sup>, V. B. Brudanin<sup>n</sup>, Y-D Chan<sup>g</sup>, V. G. Egorov<sup>n</sup>, S. R. Elliott<sup>f</sup>, V. M. Gehman<sup>f,g</sup>, T. W. Hossbach<sup>e</sup>, J. D. Kephart<sup>a,b,e</sup>, M. F. Kidd<sup>c,b,o</sup>, S. I. Konovalov<sup>m</sup>, K. T. Lesko<sup>g</sup>, Jingyi Li<sup>l</sup>, D-M Mei<sup>f,p</sup>, S. Mikhailov<sup>l</sup>, H. Miley<sup>e</sup>, D. C. Radford<sup>h</sup>, J. Reeves<sup>k</sup>, V. G. Sandukovsky<sup>n</sup>, V. I. Umatov<sup>m</sup>, T. A. Underwood<sup>j</sup>, W. Tornow<sup>c,b</sup>, Y. K. Wu<sup>l</sup>, A. R. Young<sup>a,b</sup>

<sup>a</sup>*Department of Physics, North Carolina State University, Raleigh, NC, USA*

<sup>b</sup>*Triangle Universities Nuclear Laboratory, Durham, NC, USA*

<sup>c</sup>*Department of Physics, Duke University, Durham, NC, USA*

<sup>d</sup>*Department of Physics, University of North Carolina, Chapel Hill, NC, USA*

<sup>e</sup>*Pacific Northwest National Laboratory, Richland, WA, USA*

<sup>f</sup>*Los Alamos National Laboratory, Los Alamos, NM, USA*

<sup>g</sup>*Lawrence Berkeley National Laboratory, Berkeley, CA, USA*

<sup>h</sup>*Oak Ridge National Laboratory, Oak Ridge, TN, USA*

<sup>i</sup>*Department of Physics, University of South Carolina, Columbia, SC, USA*

<sup>j</sup>*AMETEK/ORTEC, Oak Ridge, TN, USA*

<sup>k</sup>*Reeves and Sons, LLC, Richland, WA, USA*

<sup>l</sup>*Duke University Free-Electron Laser Laboratory, Durham, NC, USA*

<sup>m</sup>*Institute of Theoretical and Experimental Physics, Bol'shaya Chermushkinskaya ul. 25, Moscow, 117259 Russia*

<sup>n</sup>*Joint Institute for Nuclear Research, Dubna, Moscow oblast, 141980 Russia*

<sup>o</sup>*Tennessee Tech University, Cookeville, TN, USA*

<sup>p</sup>*University of South Dakota, Vermillion, SD, USA*

<sup>q</sup>*Princeton University, Princeton, NJ, USA*

---

## Abstract

We present data characterizing the performance of the first segmented, N-type Ge detector, isotopically enriched to 85% <sup>76</sup>Ge. This detector, based on the Ortec PT6x2 design and referred to as SEGA (Segmented, Enriched

---

\*L. E. Leviner

*Email addresses:* lelevine@ncsu.edu (L. E. Leviner), hoback@ncsu.edu (H. O. Back), aryoung@ncsu.edu (A. R. Young)

Germanium Assembly), was developed as a possible prototype for neutrinoless double beta-decay measurements by the MAJORANA collaboration. We present some of the general characteristics (including bias potential, efficiency, leakage current, and integral cross-talk) for this detector in its temporary cryostat. We also present an analysis of the resolution of the detector, and demonstrate that for all but two segments there is at least one channel that reaches the MAJORANA resolution goal below 4 keV FWHM at 2039 keV, and all channels are below 4.5 keV FWHM.

*Keywords:* double beta decay, segmented, germanium, detector, majorana, neutrinoless

---

## 1. Introduction

The Segmented Enriched Germanium Assembly (SEGA) is a prototype detector for the MAJORANA experiment that is predominately focused on the search for neutrinoless double beta-decay of  $^{76}\text{Ge}$  [1, 2, 3]. The observation of neutrinoless double beta-decay would establish that neutrinos are Majorana particles, show that lepton number is not conserved, and provide information concerning the absolute neutrino mass scale [4, 5, 6]. The ultimate goal of the MAJORANA experiment is to probe neutrinoless double beta-decay half-lives greater than  $10^{27}$  years and the absolute neutrino mass scale at 20-40 meV.

The search for such rare events requires significant effort to reduce the effects of background events, which include cosmic rays, decay events from natural and cosmogenic radioisotopes, and two-neutrino double beta-decay events. Methods to eliminate backgrounds include the use of ultra-pure materials, shielding from external sources, optimization of energy resolution, segmentation, and pulse-shape analysis (PSA). The goal of the tonne-scale MAJORANA experiment is to reduce background events to 1 count/tonne/year in an approximately 4 keV region-of-interest (ROI) centered around the  $^{76}\text{Ge}$  Q-value of 2039 keV. The MAJORANA collaboration is currently focusing development efforts towards P-type, point contact detectors [7] for the MAJORANA DEMONSTRATOR project [2, 3, 8]; however the remarkable event reconstruction and background rejection capabilities of segmented N-type detectors make them an interesting alternative [9, 10, 11]. For both of these geometries, optimum background rejection is achieved by analysis of pulse shapes to differentiate backgrounds from a potential neutrinoless double beta-decay signal. This is possible primarily because double beta-decay gives rise

to a “single-site” event in which ionization is deposited in a very small volume, with a maximum linear dimension of about a millimeter, whereas events originating from background gamma-rays typically produce multiple Compton scattering sites typically separated by a few centimeters. By analyzing the pulse-shape in each physical segment of our N-type detector, one can reconstruct and reject events which produce ionization in more than one segment or result in multiple ionization events in a single segment. A detailed analysis of the pulse-shapes and background rejection capabilities is the subject of an article in preparation [12]. For more details on background rejection strategies, refer to references [1, 10, 11].

The SEGA detector is the first  $^{76}\text{Ge}$  enriched, segmented, N-type High Purity Germanium (HPGe) detector. The GRETINA [13], AGATA [14], and GERDA [15, 16] collaborations have already demonstrated the capability of reconstructing the event topology for high-energy (near 2 MeV) events associated with double beta-decay with position resolution of a few millimeters through analysis of pulse shape and the image-charge distribution in similar, highly segmented N-type detectors. SEGA has also served as a test bench for engineering low-background crystal mounts and cryostats components for the N-type segmented geometry. Finally, after installation in a low background cryostat, SEGA should also be a valuable tool for a variety of background studies.

In this article, we report on the general characteristics and performance of the SEGA detector in a temporary cryostat. The fragility of the outer, P-type lithographic contacts presents some risk in the transfer to a permanent, low background set of contacts, so we present the preliminary performance of this system as a benchmark in our progress towards implementing a low background configuration underground. The electronic noise characteristics were not optimal, which was primarily due to “warm” preamplifiers, with long contact-to-preamplifier wires. However, our analysis of the system indicates that SEGA can meet the performance specifications for a large scale double beta-decay experiment when equipped with cold FETs, mounted as close as possible to the crystal.

## 2. The Detector

SEGA is an N-type HPGe detector enriched to 85%  $^{76}\text{Ge}$  with 6 outer, azimuthal and 2 central, axial segmentations. The Ge material used to produce SEGA was composed of three separate batches from ITEP [17], IGEX

[18], and Dubna [19], with the respective  $^{76}\text{Ge}$  enrichment abundances and masses of 87.1% [4 kg], 80.8% [3.7 kg], and 86.8% [3.3 kg]. The 1.374 kg detector has a diameter of 64.8 mm and a total length of 80.0 mm. The six outer contacts were produced by implanting the masked Ge with 100 keV  $^{11}\text{B}$  ions. The resulting inter-segment gap is 170 microns. The two internal lithium contacts are produced using novel, monolithic segmentation technology developed by ORTEC [20]. The internal contact segmentation results in a (C2) contact which is situated on the surface of a 18.2 mm diameter hole bored 58.0 mm into the crystal and a (C1) contact positioned on a 10.5 mm dimple at the bottom of the bored hole. This segmentation geometry results in 12 physical segments (six in a cylindrical geometry and six in a “hockey puck” geometry) and is referred to as the ORTEC PT6x2 geometry [21], with an idealized example depicted in Fig. 1.

A possible advantage of this scheme for double beta-decay measurements is that the resultant 12 physical segments are produced with only eight instrumented contacts, minimizing the required front-end electronics per physical segment<sup>1</sup>. We note that the resultant segment volumes were near those selected for prototype designs of the MAJORANA experiment using N-type detector arrays [1].

The labeling of the twelve physical segments of the SEGA detector follows a CXSY format, where X and Y represent one of the two central and six outer contacts, which may also be referred to as channels, respectively. In order to avoid loss of enriched Ge in this prototype detector, the closed end, outer surface of the SEGA detector was not “bulletized”, as indicated in Fig. 1, resulting in low electric fields and poorer charge collection in the corners of the closed end. Detectors used in a germanium double beta-decay experiment would be bulletized.

### 3. Test Environment

#### 3.1. Temporary Cryostat

All of the tests and performance data presented in this document were taken with the SEGA detector mounted in a temporary cryostat. The detector was mounted vertically with the central bore oriented with the hole

---

<sup>1</sup>The advantage of fewer contacts per physical segment will be partially offset by the activity of the components required for the central contacts inserted into the inner bore of the crystal.

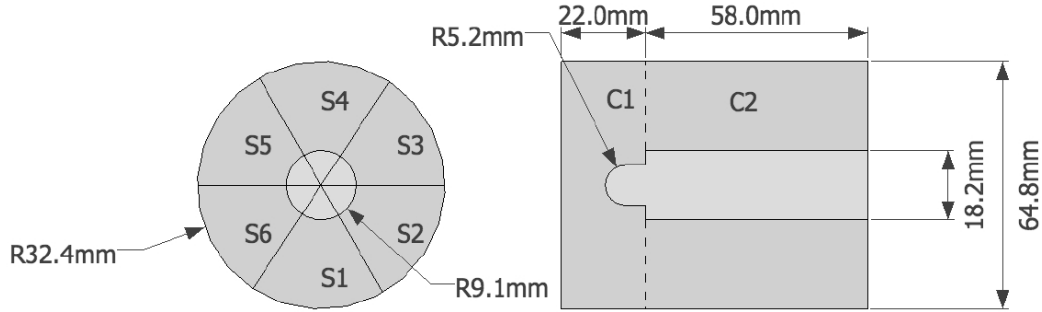


Figure 1: The ORTEC PT6x2 detector geometry. The SEGA detector is not “bulletized”, which means there is no radius for the closed-end, outer edge.

upward (C2 above C1). The outer contacts are copper leaf-springs with a  $25 \text{ mm}^2$ , 0.5 mm thick indium foil at the point of contact between the spring and the detector face. The central contacts were mounted to a brass rod which was inserted into the central bore of the detector: the C2 contacts were leaf-springs attached to the rod and the C1 contact was a gold-coated brass plug mounted on the end of the rod (with Indium foil at the point of contact with the crystal) and kept in contact with the crystal. The detector was mounted in a central shield to provide thermal isolation and held in place with PTFE pads (with Cu coated PTFE straps to provide good thermal contact with the base plate). The cryostat was configured as a dip-stick and inserted in a standard, ORTEC  $\text{LN}_2$  dewar. The temperature of the crystal was maintained at 93 to 97 K, as monitored by a platinum resistor mounted to the base plate.

The detector signals were routed out of the cryostat to HeKo preamplifiers [22, 23, 24] with warm FETs, which have an input capacitance of 15 pF and a maximum energy throughput of about 10 GeV/s. When the detector is biased, the inner segments have a calculated capacitance of 14-20 pF for C1 and 40 pF for C2, and the outer segments have calculated capacitances of 9-10 pF. The high voltage is applied to the central contacts via separate 2 G $\Omega$  load resistors with the two central contacts being AC coupled to the preamps via 2.7 nF, 6 kV ceramic capacitors. The signals were processed using two XIA DGF-4C [25] (Digital Gamma Finder with 4 Channels) modules, which digitized the signals using 14-bit, 40 MHz ADCs. These modules can store up to 100  $\mu\text{s}$  waveforms per event, perform pulse-shape analysis, and extract a real time energy using an on-board trapezoidal filter into a spectrum with

up to 32K channels. Each channel has a real-time processing unit (RTPU), which is equipped with a field programmable gate array (FPGA) and a FIFO memory. When an event is detected in the FPGA, a trigger is issued to the digital signal processor (DSP), which then processes the data and prepares it to be read out by the CAMAC interface to the computer. The system is configured to read out all eight channels when a trigger is issued in either of the 2 central-contact channels. The configuration of the system in the temporary cryostat did not accommodate instrumenting a pulser for all contacts, so the response of the detector system to external radioactive sources was used to characterize the detector performance.

## 4. Detector Properties

### 4.1. Electric-Field Profile

For Pulse-shape Analysis (PSA) studies, the electric-field profile for SEGA was calculated (see Fig. 2). An impurity concentration, based on measurements at ORTEC, which varied from  $3.0 \times 10^9/\text{cm}^3$  at the open end of the crystal to  $2.7 \times 10^{10}/\text{cm}^3$  at the closed end was used, along with no radial gradient. From this electric-field profile it is evident that the closed end has low-field regions near the edge of the crystal where charge collection is expected to be less efficient.

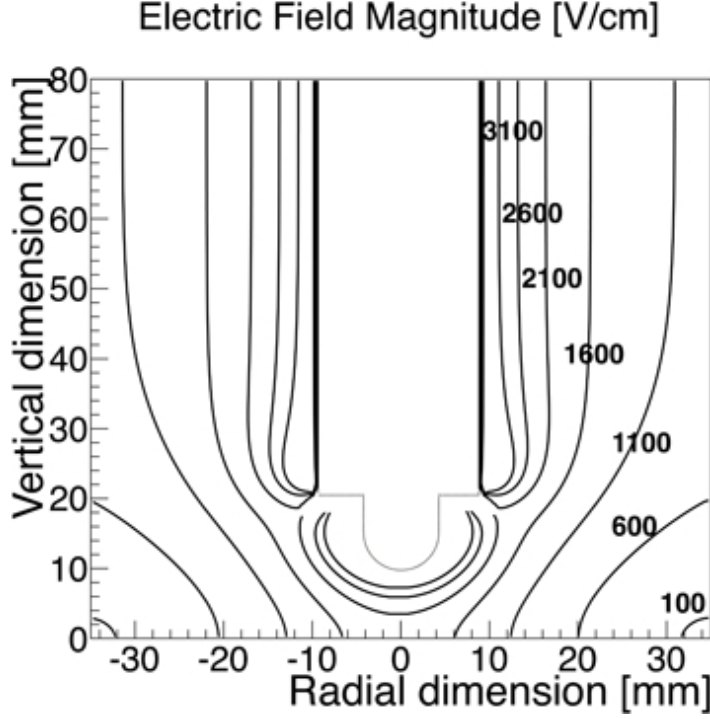


Figure 2: Calculated electric-field profile in the SEGA crystal. The inner electrode details are not shown per vendor request, hence discontinuities are present for some of the field lines.

In efforts to quantitatively assess the effects of the low-field regions, rise-time and low-energy tail analyses were done with a  $^{60}\text{Co}$  source. It was found that C1 segment's rise-time means were greater than C2 segment's rise-time means, with all segments' means ranging from 170 ns to 250 ns and less than 0.2% events having rise-times greater than 400 ns. Low-energy tails on the photopeaks were also found to be present and the degree of low-energy tailing is shown in Figs. 3 and C.7 (See Appendix C). The 1332 keV photopeaks were fit with both a Gaussian and a modified Gaussian function [26] shown below, which took into account the low-energy tail.

$$a_0 e^{-\frac{(x-a_1)^2}{2a_2^2}} + a_3 e^{-\frac{(x-a_1+a_4)^2}{(2a_2^2 a_5)}} + a_6 (\text{Erf}(a_7(x-a_1)) + 1) \quad (1)$$

As expected, due to the low-field regions, the FWHM/FWHM ratios in Table C.7 show significant deviations of the modified Gaussian functional fit from

the Gaussian functional fit for the SXC1 channels. To further support the deviations from a Gaussian functional fit, the integrated number of counts in the low-energy tail as a ratio to the number of counts in the photopeak is presented in Table C.7. The increased size of the low-energy tails for the S channels coupled to C1 as opposed to C2 is evident.

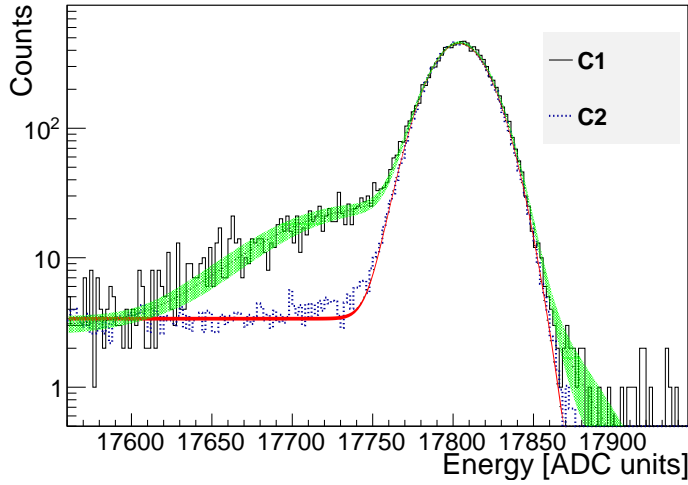


Figure 3: 1332 keV photopeak for channel S1 with S1C1 and S1C2 single segment cuts. The degree of low-energy tailing is clearly greater in the C1 segment where the low-field regions are present. The width of the fit band reflects uncertainties of the fits to the low-energy tail.

#### 4.2. Depletion Voltage

The depletion voltage was determined at ORTEC by peak efficiency measurements of the 1332 keV  $^{60}\text{Co}$   $\gamma$  rays as a function of bias voltage while connecting the two central contacts (C1 and C2). From these measurements and observations of the behavior of the central contacts which become independent only when the detector is almost fully depleted, it was determined that the depletion voltage for the crystal is 4750 V and an operating voltage of 4800 V was deemed appropriate (see Fig. 4).

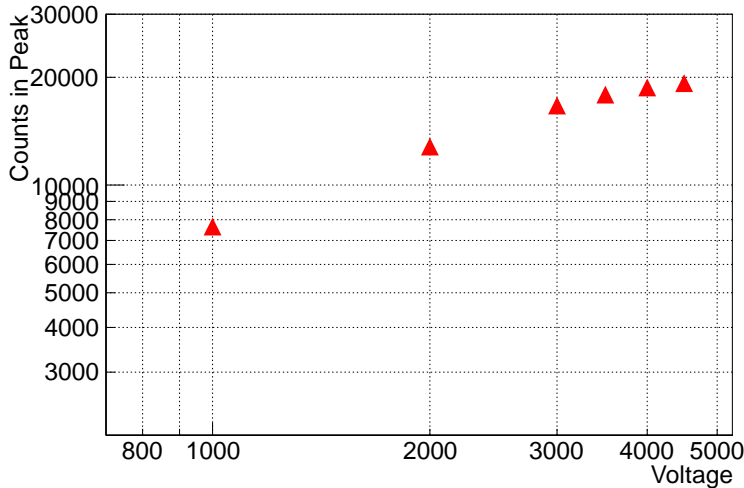


Figure 4: Counts in the  $^{60}\text{Co}$  1332 keV  $\gamma$ -ray peak (for the C1 and C2 channels connected together) as a function of bias voltage. The slope of the efficiency curve approaches zero as the operating voltage is reached, confirming that effectively all charge deposited in the detector is collected.

#### 4.3. Leakage Current

One challenge associated with the fabrication of SEGA was the reduction of the leakage current to an acceptable level. In order to accomplish this task without reprocessing all of the enriched germanium multiple times, ORTEC re-etched the surface of the crystal and produced new contacts until an “acceptably” low leakage current was obtained. Ultimately the leakage current was determined by ORTEC to be roughly 350 pA by connecting together all of the outer contacts (S1-S6) and measuring the current to ground with a bias voltage of 4800 V applied to the central contacts C1 and C2. Even so, this leakage current was about factor of two above what ORTEC considered “optimal”. It should be noted that, ORTEC also performed similar leakage current measurements of a non-enriched prototype detector with the PT6x2 geometry and found the leakage current to be 72 pA and 80 pA at 3200 V and 3300 V respectively [21, 27]<sup>2</sup>. For a quantitative treatment of the impact of leakage current on the resolution see Sec. 4.7 and Appendix B.

<sup>2</sup>3200 V was the operating voltage of the non-enriched prototype PT6x2 detector.

Additional measurements of the leakage current for each segment were performed at Triangle Universities Nuclear Laboratory (TUNL) soon after receiving the SEGA detector from ORTEC. For these measurements the detector was fully biased and left overnight, since it was found the leakage current would decrease significantly after the first few hours after applying bias to the detector. The following morning, the voltage was slowly stepped down and the leakage current measured through each outer segment after the current was allowed to settle for approximately 15 minutes. From this study it was found that the dominant source of leakage current was segment S4 (see Fig. 5). This overall pattern (segment S4 being the dominant source of leakage current) was maintained over the 10 year period for which the measurements documented in this work were performed. However, there was a significant increase in the magnitude of the leakage current over this period (see Sec. 4.7 and Appendix B for details).

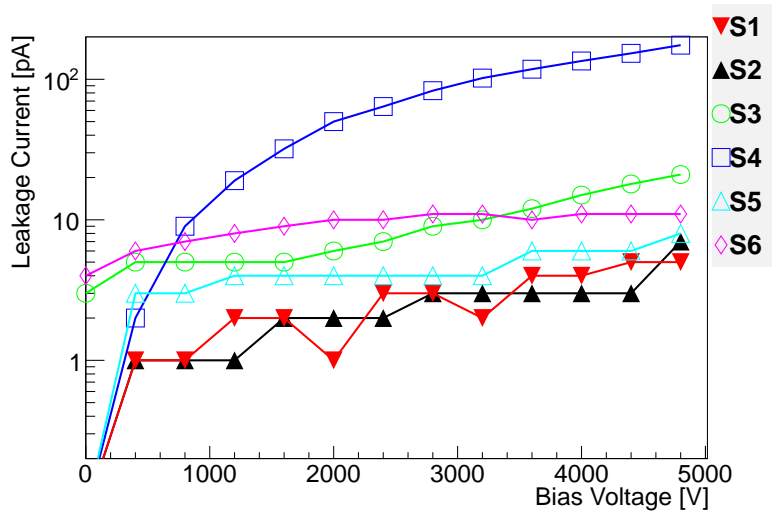


Figure 5: Leakage current from segments S1 to S6 as a function of bias applied to C1 and C2. These measurements were done in February, 2003.

#### 4.4. Efficiency

In order to assess the active volume within the detector, the intrinsic peak efficiency was measured using a  $3.15 \mu\text{Ci } ^{60}\text{Co}$  source. First, by scanning with a  $^{57}\text{Co}$  source it was determined that the crystal, within the cryostat, was positioned 4.1 cm from the endcap. Then, the  $^{60}\text{Co}$  source was placed

approximately 25 cm above the top of the crystal. It should be noted that this method is slightly different from the IEEE standard efficiency measurement [28] where the source is placed 25 cm from the endcap. Data were recorded for approximately 43 hrs to reduce the statistical uncertainty in the sum-peak to less than 5%. The rate was approximately 700 Hz with our system livetime near 20%, which was limited by the throughput of the CAMAC controller. For these data the trapezoidal filter rise and gap times were set to 10.8  $\mu$ s and 1.6  $\mu$ s respectively (corresponding to an effective shaping time of approximately 6  $\mu$ s for semi-Gaussian filters) [25].

To determine the full energy deposited within the detector for a given event, the energy for each of the outer S channels (S1-S6) were summed, and because of the coupling between segments, a cross-talk correction [29] was applied (see Fig. 10 in Sec. 4.6). By analyzing the number of counts in the two  $^{60}\text{Co}$   $\gamma$  peaks and in their sum-energy peak (2505 keV), it was possible to determine the intrinsic peak efficiency at 1173 keV and 1332 keV, which were  $13.9\pm 1.7\%$  and  $12.8\pm 1.3\%$  respectively, where the error value is dominated by a 5% uncertainty in the source and detector relative positioning. Sum-coincidence and angular correlation effects were accounted for in this study, while the effect of system dead time was avoided using the sum-peak method. These measurements were found to be in reasonable agreement with a simulation of the as built SEGA detector geometry using the MaGe package [30], which yielded values of  $14.9\pm 0.3\%$  and  $13.8\pm 0.2\%$  respectively. The simulated geometry is depicted in Fig. 6. For 1332 keV the measured and simulated efficiency values relative to a 7.62 cm diameter  $\times$  7.62 cm length NaI(Tl) detector are  $108\pm 11.0\%$  and  $115\pm 1.7\%$  respectively.

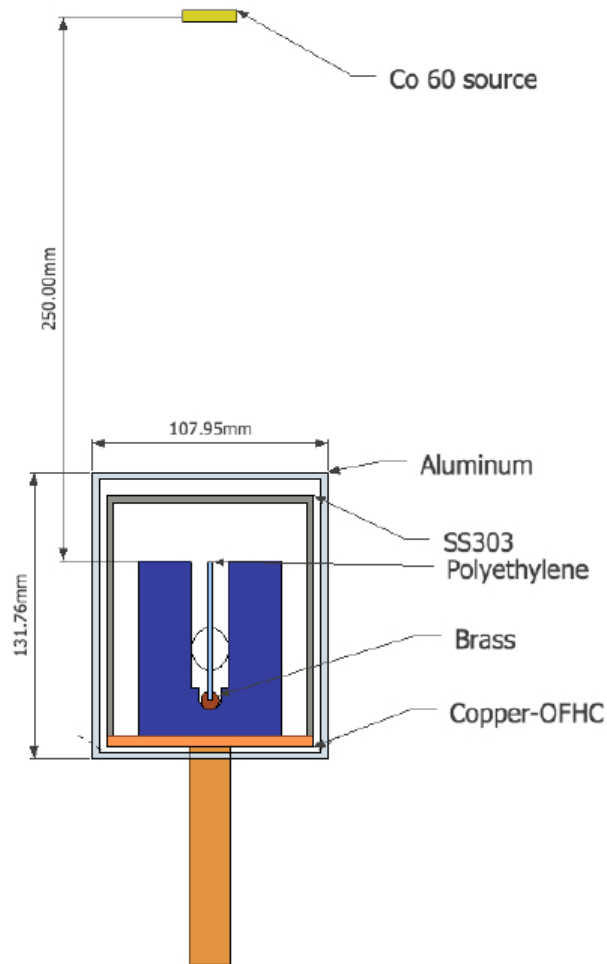


Figure 6: SEGA detector geometry used in MaGe simulation. The cold finger and some small parts were not simulated.

#### 4.5. Calibration and detector linearity

Energy measurements were either made using the trapezoidal filter in the XIA, DGF-4C module [31], or in some special cases, directly from trace data. The XIA trapezoidal filter is designed to be relatively insensitive to the signal rate and uses a large running sample of the baseline to accurately determine its contributions to the filter sums. The filter takes as input the preamplifier

decay times (approximately 48  $\mu$ s), which were determined by fitting large samples of 40  $\mu$ s long traces for each segment.

The system linearity was analyzed using the same data set from the efficiency study and fitting to the various background and  $\gamma$ -ray lines listed in Table 1 using a Gaussian function with a linear background. The centroids from the Gaussian fits to the peaks were then fit with a linear function. The results are depicted in Fig. 7, where we note that the y-intercepts were all smaller than 0.56 keV and the integral linearity was better than 0.067% at one sigma level for all channels.

We also note the detector was calibrated a number of times (over a period of 10 years) using linear and quadratic functions along with a variety of lines. There was almost no variation in the extracted calibration parameters and the quadratic terms were less than  $4.2 \times 10^{-9}$  keV resulting in corrections of less than 0.2% to the calibrated energy values out to 2039 keV.

Source	Energy [keV]
$^{214}\text{Bi}$	351.932
$^{214}\text{Bi}$	609.312
$^{60}\text{Co}$	1173.237
$^{60}\text{Co}$	1332.501
$^{40}\text{K}$	1460.830
$^{214}\text{Bi}$	1764.494
$^{208}\text{Tl}$	2614.533

Table 1:  $\gamma$ -ray sources used for system linearity evaluation.

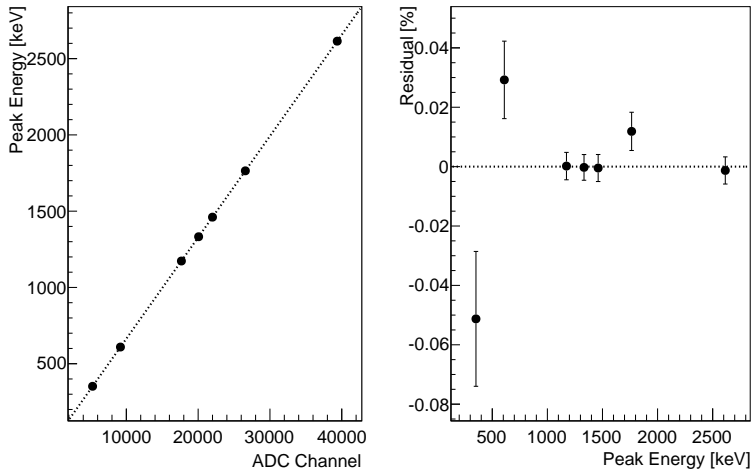


Figure 7: Energy response of C2 channel for C2S2 events from a  $^{60}\text{Co}$  source and various background sources, along with the residuals of the data-points from the linear fit.

#### 4.6. Cross-talk

Two different methods were used to determine integral cross-talk. One required selecting events where all of the  $\gamma$ -ray energy deposition is in one physical segment and measuring the shifts in the measured energy in the non-triggered channels (band method). Another required the construction of so-called “superpulses”, which are the average pulses of many events of the same energy deposition and segment. For this analysis both methods were used.

For the band method it was first necessary to develop single-segment cuts where only two channels, a central contact and an outer contact, had an energy value greater than the nominal threshold of about 700 keV. The other channels should have a measured energy value of zero, but due to cross-talk this is not necessarily true. By performing single-segment cuts and plotting the triggered channel’s energy *versus* each non-triggered channel’s energy, cross-talk bands become apparent (see Fig. 8) and fitting to the slope of the cross-talk bands provides the cross-talk coefficients necessary to account for this effect [29].

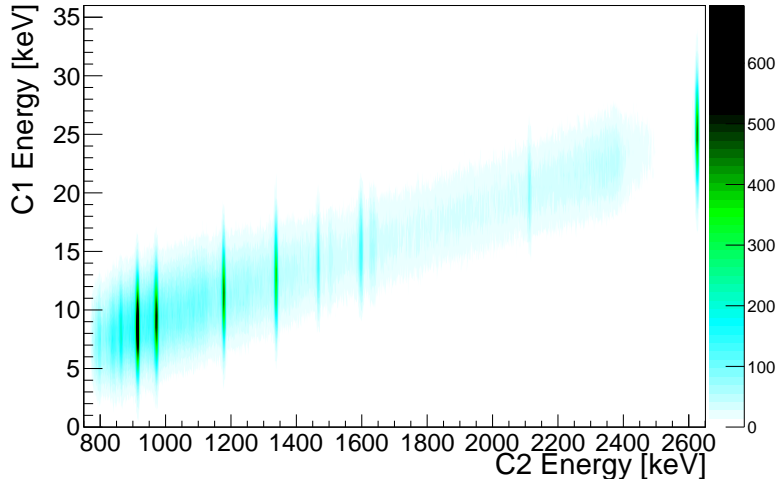


Figure 8: Cross-talk band in C1 for C2S2 events.

A few issues complicated this analysis. An initial problem was that the threshold value settings in the XIA DGF-4C module for these data were around 700 keV and channels which were not over threshold had an XIA energy filter value of zero. This was a problem because energies of just a few keV are characteristic of cross-talk between contacts. It was also necessary to avoid spurious triggers and incorrect integrated energy values reported by the XIA DGF-4C module when large image charge was present. To address these issues the trace from each channel was used to determine the energy using an offline trapezoidal filter [31]. This filter is similar to the trapezoidal filter the XIA DGF-4C module uses to calculate the energy, but results in lower resolution because the trace samples used for this particular study were  $3 \mu\text{s}$  long and included only about 300 ns of baseline data. The filter resulted in about a factor of two poorer resolution than the XIA energy filter, but did not impact the cross-talk measurement.

The second method involved the construction of “superpulses”, which are constructed for all segments, in which one produced an averaged record for the charge induced by the triggering segment in each preamplifier [32]. In order to develop superpulses it was first necessary to perform single segment cuts for each segment and cut for events for which the entire  $\gamma$ -ray energy is deposited in the triggered segment. The events’ traces were then averaged

together to form a superpulse for each individual channel (see Fig. 9). The superpulses were then digitally shaped using the offline trapezoidal filter and the average energy value was calculated. To acquire the cross-talk coefficients superpulses were constructed for several  $\gamma$ -ray energies providing an energy dependent response curve for each individual channel, which was fit using a two parameter linear function. The slope determined by the fit is the cross-talk coefficient. The difference between the two methods is that in the superpulse method, cuts are applied around the full peak  $\gamma$ -ray energy and not the cross-talk band itself.

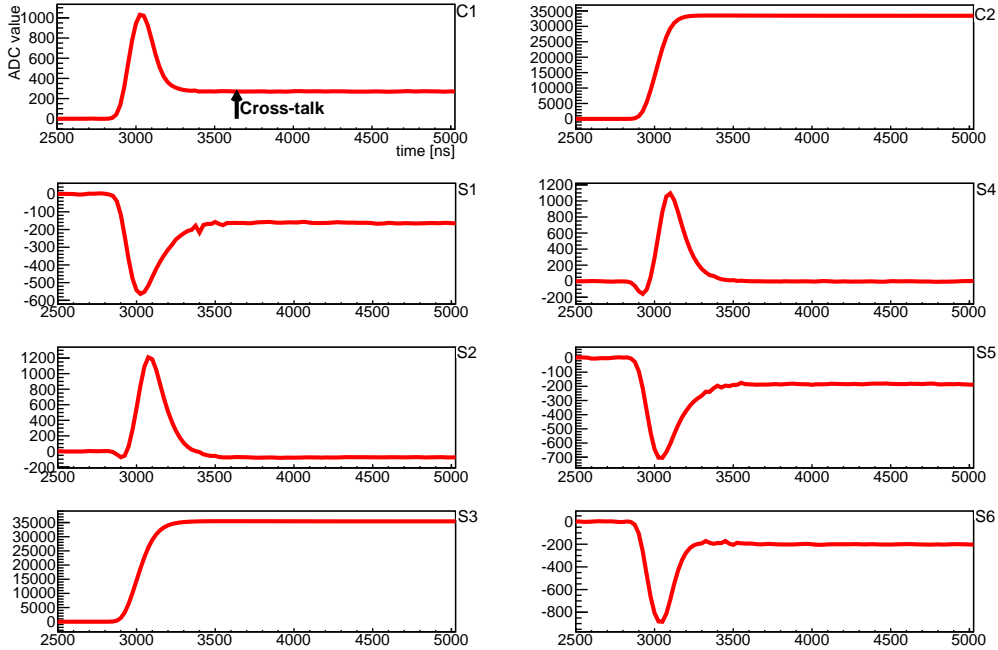


Figure 9: Superpulses (ADC values *versus* time) from each preamplifier channel for  $^{60}\text{Co}$  1332 keV  $\gamma$ -ray events in segment C2S3. C2 and S3 show a clear charge from an event, while the overall non-zero charge in channels C1, S1, S2, S4, S5, and S6 indicate cross-talk between channels.

From these two methods it is possible to determine seventy-two cross-talk coefficients of the  $12 \times 8$  cross-talk matrix, where the remaining twenty-four are folded in with the calibration. The values obtained (See Table A.4 in Appendix A) using both methods are acceptable and reflect the current op-

erating status of SEGA. Most of the coefficients were less than 1%, which is consistent with cross-talk values reported for other, segmented detectors [13, 29]. However, there was significant cross-talk between the two central contacts whenever there was an event in the upper C1 segment of the detector. This is expected from the geometry of the inner contacts and does not pose a significant problem for signal analysis.

An example of applying the cross-talk correction is shown in Fig. 10 where we have summed the outer S channels' (S1-S6) energies. Without applying the cross-talk correction we see similar cross-talk effects as the AGATA collaboration [29] where the photopeak's FWHM increases and the peak's position is shifted lower in energy as the multiplicity increases. Using the cross-talk coefficients listed in Table A.4 in Appendix A, we are able to re-align and reconstruct the photopeaks.

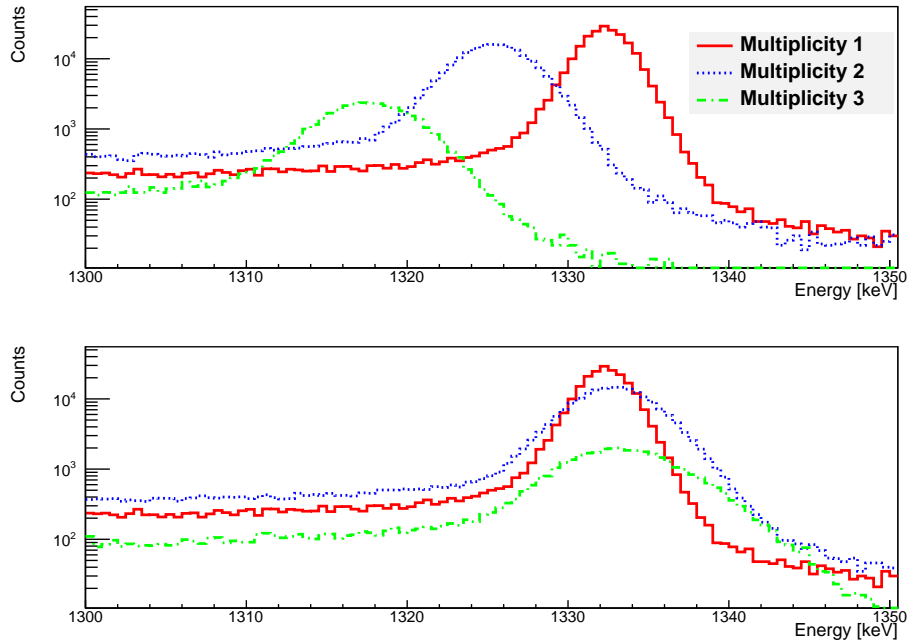


Figure 10: Total energy determined by summing the outer S channels (S1-S6) energies before (top) and after (bottom) the cross-talk correction was applied for multiplicities 1, 2, and 3.

#### 4.7. Electronic Noise

Noise contributions to the energy resolution (expressed as the FWHM of the  $\gamma$ -ray full energy) are specified in terms of equivalent noise charge (ENC in units of  $e$ ). ENC can be converted to energy resolution by the following [33]

$$FWHM(eV) = 2.35 \cdot 2.96 \left( \frac{eV}{e} \right) \cdot ENC(e). \quad (2)$$

As shown by [34] the ENC introduced due to the detector-preamplifier noise sources can be represented as

$$ENC^2(e_{rms}^2) = \frac{h_1}{\tau} + h_2 + h_3\tau \quad (3)$$

$$h_1(e^2 \mu s) = aC_{tot}^2 A_1 \quad (4)$$

$$h_2(e^2) = \left( 2\pi a_f C_{tot}^2 \frac{b_f}{2\pi} \right) A_2 \quad (5)$$

$$h_3\left(\frac{e^2}{\mu s}\right) = bA_3, \quad (6)$$

where  $\tau$  is the peaking time of the shaping network,  $a$  is the series white noise,  $b$  is the parallel white noise,  $a_f$  and  $b_f$  are the non-white series and parallel noise,  $C_{tot}$  is the total input capacitance, and  $A_1$ ,  $A_2$ , and  $A_3$  are weighting factors dependent upon the shaping network that can be found in [35]<sup>3</sup> (See also Appendix B).

Our objective was to quantify the noise sources by varying the peaking time of our shaping network. Typically a pulser is used to decouple the additional contributing factors to the measured peak width, but since SEGA currently is not equipped with a pulser we placed a  $^{60}\text{Co}$  source above the crystal and recorded data with very long traces (40  $\mu\text{s}$ ). Having 40  $\mu\text{s}$  traces allowed us to apply an offline digital trapezoidal filter outlined in [31], which is the same filter implemented in the XIA module, while varying the shaping parameters, eliminating the need for multiple data sets for which the shaping parameters were varied from run to run. FWHM values were measured by fitting the 1332 keV photopeak in the trapezoidal filter output spectra using a Gaussian function with a linear background. To obtain only the electronic noise contribution to the photopeak width all other components, including

---

<sup>3</sup>The  $A_1$ ,  $A_2$ , and  $A_3$  values for a trapezoidal filter are 2.00, 1.38, and 1.67 respectively.

charge creation statistics and charge collection efficiency were removed using the coefficients obtained from the resolution versus energy model presented in the following section. The  $ENC^2$  versus  $\tau$  curves in Fig. 11 provide some insight to how the three noise sources contribute individually to the peak width.

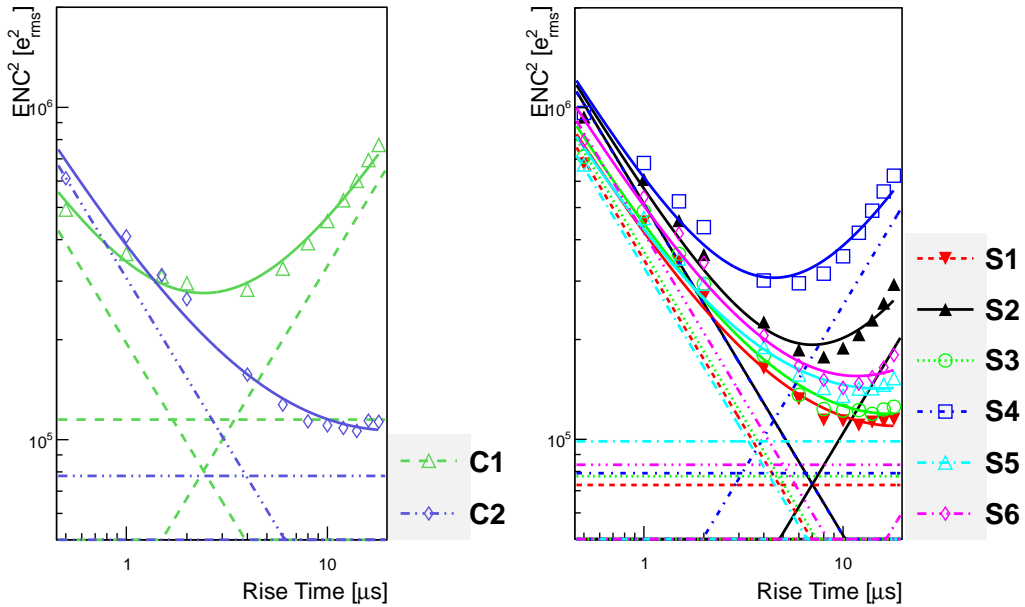


Figure 11: For each readout contact, we depict  $ENC^2$  versus rise-time curves along with the fitted contributions for white series, white parallel and non-white noise (see coded legend at right of figure; noise components are represented by dashed/dotted lines with exception to S2 being solid). The peaking time for a trapezoidal filter shaping network is its rise-time [35].

Of the three noise contributions it is evident that the parallel noise exhibits the most non-uniformity from channel to channel and is the dominant noise source for a few channels at rise times longer than  $7 \mu s$ . It is also clear that the current system is limited by the series noise component and significant improvement of this component is expected with the transfer to an optimized cryostat. A more detailed treatment of the parallel noise component is included in Appendix B.

#### 4.8. Resolution

Due to the risk associated with each installation of a new set of contacts, a significant effort was made to evaluate the performance of the SEGA detector in its temporary cryostat. At the current noise levels microphonics were found to be negligible, but the overall electronic noise (due to a combination of grounding and shielding issues) was significant and not optimal.

The resolution was measured using a conventional spectroscopic amplifier with several different shaping times, the on-board energy filter of the XIA DGF-4C module and an offline implementation of a trapezoidal filter. For the data presented in Fig. 12 and Tables 3 and C.7 the trapezoidal filter rise and gap times were set to 6.0  $\mu\text{s}$  and 1.2  $\mu\text{s}$ , respectively. The sources used for the resolution measurements along with the measured rate, livetime, and  $\gamma$ -ray peaks used for each source are listed in Table 2.

Source	Measured Rate [counts/s]	Livetime %	Peaks [keV]
$^{57}\text{Co}$	577	25.5	122
$^{60}\text{Co}$	1880	6.6	1173, 1332
$^{137}\text{Cs}$	353	41.2	662
Th	86	65.1	911, 1764, 2615

Table 2: Sources used for resolution study.

Since each physical segment is unique, it was necessary to perform resolution measurements of both read-outs (central and outer) for each physical segment. Full width at half maximum (FWHM), full width at tenth maximum (FWTM), and full width at fifty maximum (FWFM) values were determined by fitting photopeaks using both a Gaussian function and modified Gaussian function. Results of these measurements are shown in Table C.7 in Appendix C.

The resolution measurements were interpreted to quantify the factors that contribute to the photopeak width and included: the inherent statistical spread in the number of charge carriers ( $W_D$ ), variations in the charge-collection efficiency ( $W_X$ ), and contributions from electronic noise ( $W_E$ ). Since each of these three terms has a Gaussian distribution, they add in quadrature and the photopeak width can be composed of these terms as follows

$$W_T^2 = W_D^2 + W_X^2 + W_E^2. \quad (7)$$

$$W_T^2 = aE + bE^2 + c. \quad (8)$$

The charge-creation process factor is inherent to the material and is given by

$$W_D^2 = (2.35)^2 F \epsilon E \quad (9)$$

where  $F$  is the Fano factor,  $\epsilon$  is the average energy needed to create an electron-hole pair, and  $E$  is the incident  $\gamma$ -ray energy [33]. A range of Fano factor values exist in the literature, but for the data presented in Fig. 12 and Table 3 the Fano factor value of 0.11 was used [36]. The completeness of charge-collection term,  $W_X^2$  (the term proportional to  $b$  in Eq. 7), is quadratic in terms of the incident  $\gamma$ -ray energy and is a property of the detector geometry and impurity profile. As expected, charge trapping varies throughout the detector volume and it is exacerbated in regions where the electric field is small. The influences from charge trapping are especially apparent in the C1 physical segment where the electric fields are low. The final contribution to the peak width is the electronic noise of the system which does not vary with the incident  $\gamma$ -ray energy (See Table 3 for fit values of the  $W_X^2$  and  $W_E^2$  terms).

Given this model of how the resolution should vary with incident  $\gamma$ -ray energy, the evaluated peak widths were fit with a second order polynomial as a function of  $\gamma$ -ray energy, which allowed us to assess the contributing factors to the photopeak width. In efforts to establish a fixed Fano factor value for all channels, values from 0.06 to 0.13 were tested. It was determined that varying the Fano factor value within this range only changed the measured and projected FWHM values at 2040 keV by less than 0.9% and 2.1% respectively.

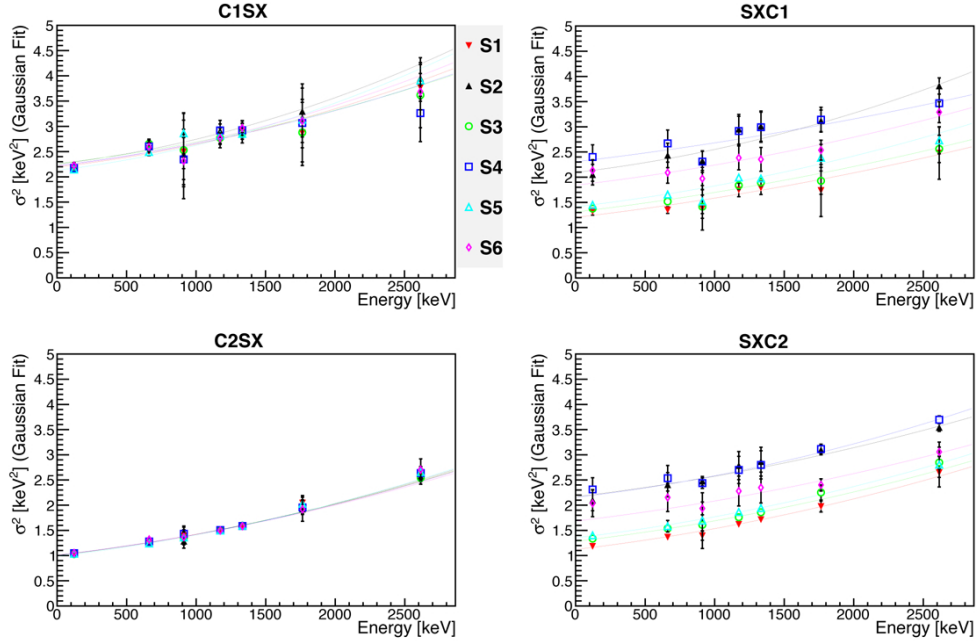


Figure 12:  $\sigma^2$  versus energy for Gaussian fits to the full-energy peak for all physical segments. The solid curves are the result of fits for a quadratic model for  $\sigma^2$  as a function of energy. The sources used for this study are listed in Table 2.

During the evaluation of the resolution data it was found that three of the outer channels' resolution performance exhibited higher rate sensitivity. The source of this behavior is currently unclear, but to account for this 10% error bars were placed on the higher-rate data for these channels. Following this, the error bars were increased by a calculated scale factor in order to reduce the  $\chi^2/\text{dof}$  to one. From these fits the coefficients provide a characterization of the contributing factors to the photopeak width. The extrapolated electronic noise and charge-collection terms for each channel are listed in Table 3.

Segment	$W_E^2$ (FWHM <sup>2</sup> ) [keV <sup>2</sup> ]	$W_X^2$ (FWHM <sup>2</sup> ) [keV <sup>2</sup> ]	FWHM (2040 keV) Measured [keV]	FWHM (2040 keV) Projected [keV]
C1S1	12.1 ± 0.2	2.88 ± 0.70	4.32 ± 0.08	2.75 ± 0.14
C1S2	12.4 ± 0.3	3.81 ± 1.10	4.46 ± 0.12	2.91 ± 0.19
C1S3	12.5 ± 0.4	2.35 ± 1.60	4.30 ± 0.19	2.65 ± 0.32
C1S4	12.3 ± 0.4	2.50 ± 1.50	4.30 ± 0.18	2.68 ± 0.30
C1S5	11.8 ± 0.2	3.90 ± 0.70	4.40 ± 0.08	2.93 ± 0.13
C1S6	12.2 ± 0.2	3.16 ± 0.84	4.36 ± 0.10	2.80 ± 0.16
C2S1	5.54 ± 0.08	2.09 ± 0.26	3.36 ± 0.04	2.60 ± 0.05
C2S2	5.53 ± 0.05	2.18 ± 0.16	3.37 ± 0.03	2.62 ± 0.03
C2S3	5.54 ± 0.07	2.12 ± 0.24	3.37 ± 0.04	2.61 ± 0.05
C2S4	5.55 ± 0.08	2.06 ± 0.24	3.36 ± 0.04	2.59 ± 0.05
C2S5	5.44 ± 0.06	2.29 ± 0.20	3.38 ± 0.03	2.64 ± 0.04
C2S6	5.58 ± 0.12	1.95 ± 0.37	3.35 ± 0.06	2.57 ± 0.08
S1C1	6.63 ± 0.29	1.34 ± 1.20	3.41 ± 0.18	2.45 ± 0.26
S2C1	11.6 ± 0.6	3.02 ± 0.71	4.27 ± 0.11	2.77 ± 0.21
S3C1	7.23 ± 0.15	1.44 ± 0.66	3.51 ± 0.10	2.47 ± 0.14
S4C1	12.7 ± 0.7	1.14 ± 0.80	4.19 ± 0.13	2.41 ± 0.27
S5C1	7.80 ± 0.13	2.05 ± 0.53	3.68 ± 0.08	2.59 ± 0.11
S6C1	10.2 ± 0.6	1.73 ± 0.84	3.95 ± 0.13	2.53 ± 0.24
S1C2	6.19 ± 0.07	2.02 ± 0.20	3.45 ± 0.03	2.59 ± 0.04
S2C2	12.0 ± 0.4	1.85 ± 0.40	4.18 ± 0.07	2.55 ± 0.14
S3C2	7.08 ± 0.08	1.89 ± 0.25	3.56 ± 0.04	2.56 ± 0.05
S4C2	11.9 ± 0.5	2.36 ± 0.42	4.23 ± 0.07	2.65 ± 0.15
S5C2	7.47 ± 0.30	2.10 ± 0.90	3.64 ± 0.13	2.60 ± 0.19
S6C2	9.31 ± 0.55	1.67 ± 0.51	3.83 ± 0.10	2.52 ± 0.18

Table 3: Measured electronic noise and charge-collection contributions to the photopeak width along with the measured and projected FWHM values at 2040 keV for 6  $\mu$ s rise time. The projected values assume 1.0 keV FWHM for the electronic noise contribution and the charge-collection contribution was calculated at 2040 keV. Errors are statistical uncertainties from Gaussian fits to the photopeaks and the errors from the extracted values for the  $W_E^2$  parameter.

## 5. Discussion and Analysis

The performance of this prototype detector must be evaluated in terms of how it would perform in a double beta-decay experiment. Most of the performance specifications are already within reasonable limits. The crystal impurity concentrations were near the limits of what is typically considered useful detector material at ORTEC; the bias potential was quite close to ORTEC's practical working limit of 5 kV. It is assumed that this applies

specifically to the crystal pulled for SEGA, and not to  $^{76}\text{Ge}$ -enriched material in general.

The availability of a strictly limited amount of  $^{76}\text{Ge}$  (as opposed to full-scale, enriched Ge detector development) restricted the amount of processing and the achieved operational parameters of this detector, and resulted in accepting rather high leakage currents and the lack of bulletization. The leakage currents resulted in one physical segment S4, exhibiting parallel noise which limited its resolution for shaping times longer than  $7\ \mu\text{s}$  (Sec. 4.7 and Appendix B). The lack of bulletization resulted in poorer charge collection characteristics for the C1-coupled segments relative to the C2-coupled segments, as evidenced by larger low-energy tails in the C1-coupled segments (Sec. 4.1 and Appendix C) and the larger  $W_X^2$  parameter in the behavior of the resolution as a function of energy (Sec 4.1 and Appendix C). Clearly, both leakage currents and lack of bulletization had some impact on the resolution, but do not seem to be a serious, intrinsic impediment for this geometry.

On the other hand, the only significant issue which emerged for this detector is its marginal achievement of the resolution specification (4 keV FWHM at 2039 keV). Even allowing for the degradation in performance due to leakage currents and lack of bulletization, Table 3 shows that all but two physical segments have at least one readout which meets the nominal MAJORANA resolution goal and are within the detector resolution range for the Heidelberg-Moscow experiment [37]<sup>4</sup>. These segments, C1S2 and C1S4, should also reach the MAJORANA resolution goal if somewhat shorter, optimal rise time values were used for channel C1, so we conclude all physical segments have at least one channel satisfying the minimal requirement for the MAJORANA project. We also note that the non-enriched prototype PT6x2 with cold FETs had a much smaller FWHM measured for the C1 channel at 122 keV (0.9 keV) and generally improved resolution relative to SEGA at 1332 keV (all S channel FWHM values at 1332 keV were less than 3.2 keV and the C2 channel had a FWHM value at 1332 keV of 2.4 keV) [21], indicating that detectors with the PT6x2 geometry should, in general, meet the MAJORANA resolution goal.

The performance of SEGA with cold FETs can be projected. From the resolution versus energy scan, it is clear that the energy resolution is limited primarily by electronic noise. The shaping time scans show that for the

---

<sup>4</sup>Table C.7 in Appendix C shows all channels have a FWHM at 1332 keV of at least 0.6 keV greater than the IGEX detectors [38].

S4 and possibly C1 channels, the electronic noise can be attributed primarily to the leakage current. All segments however, also exhibit series noise contributions which limit the resolution at shaping times less than 10  $\mu$ s, consistent with the attribution of large electronic noise due to the shielding and grounding issues in the temporary cryostat.

The noise contribution for a standard detector with properly grounded, shielded, and cooled FETs should be below roughly 0.7 keV FWHM. ORTEC estimates 1.0 keV may be appropriate for warm FETs. Comparing the parameters from the  $\sigma^2$  fits, one can develop an understanding of how large the noise contributions are due to the warm FETs and the temporary cryostat. In every case, larger noise contributions are observed than expected in an optimal system. The C1 and C2 channels currently have noise widths (FWHM) around 3.3 keV and 2.3 keV, respectively. The outer channels S1-S6 have a large range in noise widths of 2.5-3.3 keV. By transferring the crystal to an improved cryostat, the series noise contribution should be significantly reduced, and reach the targeted resolution of below 4 keV FWHM at 2039 keV for all channels. Table 3 provides the current measured FWHM at 2040 keV along with the projected FWHM if 1.0 keV electronic noise is assumed.

For the SEGA PT6x2 detector, the assumption that 1.0 keV electronic noise is achievable for the channels where leakage current is the dominant electronic noise source may be overly optimistic. Even for these channels, however, only about a 5% improvement in the current resolution is required to reach the MAJORANA resolution goal. This should certainly be achievable with optimized grounding, shielding, shaping parameters and cold FETs.

The fact that the leakage current flows predominately through the internal C1 contact along with the leakage current measurements of the non-enriched prototype PT6x2 detector could suggest that the leakage current behavior in SEGA may be a characteristic of the PT6x2 fabrication procedure. As pointed out in Sec. 4.3, the etching of SEGA to reduce leakage current was curtailed to preserve enriched material. Given the reasonable resolution performance of SEGA, it is expected that it will be possible to consistently meet acceptable leakage current limits if manufacturers operate in a “production” mode where stringent leakage current specifications can be applied to enriched crystals. In this case, crystals can be etched until leakage currents fall below a reasonable upper limit or the entire crystal can be returned to raw germanium to be reprocessed. This conclusion is supported by the performance of the existing PT6x2 prototype, which demonstrated acceptable resolution specifications.

## 6. Conclusion

We have reported on the successful fabrication, for the first time, of an isotopically enriched segmented N-type germanium detector. From the studies presented here and background rejection studies performed, in part, at the HIGS facility at the Triangle Universities Nuclear Laboratory [12], we believe the PT6x2 geometry is a potentially viable prototype for an N-type germanium detector experiment to search for neutrinoless double beta-decay [11, 39, 40].

## Acknowledgments

We would like to thank the TUNL technical staff for their many contributions towards this project. We would also like to acknowledge helpful discussion and feedback from A. W. Poon and R. D. Martin in the process of preparing this manuscript. This work was supported in part by the Office of Science of the US Department of Energy (DOE) under grant number DE-FG02-97ER41042.

## Appendix A. Cross-talk

The  $12 \times 8$  integral cross-talk matrix listed in Table A.4 was generated using the superpulse method described in the cross-talk section (the cross-talk matrix from the band method is in agreement with Table A.4 and excluded to avoid redundancy). Seventy-two of the ninety-six coefficients were determined from the fits to the response curves while the remaining twenty-four are folded in with the calibration coefficients and are represented by unity.

	S1	S2	S3	S4	S5	S6	C1	C2
C1S1	1	$-0.007 \pm 0.001$	$-0.009 \pm 0.001$	$-0.009 \pm 0.001$	$-0.009 \pm 0.001$	$-0.007 \pm 0.001$	1	$0.033 \pm 0.001$
C1S2	$-0.008 \pm 0.002$	1	$-0.007 \pm 0.001$	$-0.009 \pm 0.001$	$-0.009 \pm 0.001$	$-0.009 \pm 0.001$	1	$0.034 \pm 0.001$
C1S3	$-0.007 \pm 0.002$	$-0.009 \pm 0.001$	1	$-0.006 \pm 0.002$	$-0.009 \pm 0.001$	$-0.009 \pm 0.001$	1	$0.034 \pm 0.001$
C1S4	$-0.009 \pm 0.001$	$-0.009 \pm 0.001$	$-0.007 \pm 0.001$	1	$-0.010 \pm 0.001$	$-0.009 \pm 0.001$	1	$0.035 \pm 0.002$
C1S5	$-0.009 \pm 0.001$	$-0.009 \pm 0.001$	$-0.009 \pm 0.001$	$-0.005 \pm 0.002$	1	$-0.007 \pm 0.001$	1	$0.039 \pm 0.001$
C1S6	$-0.009 \pm 0.001$	$-0.008 \pm 0.001$	$-0.010 \pm 0.001$	$-0.009 \pm 0.001$	$-0.003 \pm 0.001$	1	1	$0.078 \pm 0.003$
C2S1	1	$-0.005 \pm 0.001$	$-0.007 \pm 0.001$	$-0.004 \pm 0.001$	$-0.007 \pm 0.001$	$-0.006 \pm 0.001$	$0.010 \pm 0.001$	1
C2S2	$-0.007 \pm 0.001$	1	$-0.005 \pm 0.001$	$-0.005 \pm 0.001$	$-0.006 \pm 0.001$	$-0.007 \pm 0.001$	$0.010 \pm 0.001$	1
C2S3	$-0.007 \pm 0.001$	$-0.006 \pm 0.001$	1	$-0.002 \pm 0.002$	$-0.006 \pm 0.001$	$-0.005 \pm 0.001$	$0.010 \pm 0.001$	1
C2S4	$-0.007 \pm 0.001$	$-0.007 \pm 0.001$	$-0.005 \pm 0.001$	1	$-0.008 \pm 0.001$	$-0.007 \pm 0.001$	$0.010 \pm 0.001$	1
C2S5	$-0.006 \pm 0.001$	$-0.007 \pm 0.001$	$-0.006 \pm 0.001$	$-0.002 \pm 0.001$	1	$-0.006 \pm 0.001$	$0.010 \pm 0.001$	1
C2S6	$-0.007 \pm 0.001$	$-0.007 \pm 0.001$	$-0.006 \pm 0.001$	$-0.005 \pm 0.001$	$-0.006 \pm 0.001$	1	$0.010 \pm 0.001$	1

Table A.4: Integral cross-talk coefficients.

## Appendix B. Electronic Noise

Electronic noise coefficients from the fits to the ENC<sup>2</sup> *versus* rise-time curves are listed in Table B.6. These coefficients characterize the three electronic noise components of the detector-preamplifier system, which include series, non-white and parallel noise.

Segment	h1 [ $e^2\mu\text{s}$ ]	h2 [ $e^2$ ]	h3 [ $e^2/\mu\text{s}$ ]
S1	$3.48\text{e}+05 \pm 6\text{e}+03$	$5.77\text{e}+04 \pm 3\text{e}+03$	$976 \pm 3\text{e}+02$
S2	$5.14\text{e}+05 \pm 9\text{e}+03$	$3.13\text{e}+04 \pm 6\text{e}+03$	$1.04\text{e}+04 \pm 5\text{e}+02$
S3	$3.68\text{e}+05 \pm 7\text{e}+03$	$6.22\text{e}+04 \pm 4\text{e}+03$	$1.19\text{e}+03 \pm 3\text{e}+02$
S4	$5.12\text{e}+05 \pm 1\text{e}+04$	$6.39\text{e}+04 \pm 7\text{e}+03$	$2.54\text{e}+04 \pm 7\text{e}+02$
S5	$3.3\text{e}+05 \pm 7\text{e}+03$	$8.35\text{e}+04 \pm 4\text{e}+03$	$1.44\text{e}+03 \pm 3\text{e}+02$
S6	$4.19\text{e}+05 \pm 8\text{e}+03$	$6.87\text{e}+04 \pm 5\text{e}+03$	$3.04\text{e}+03 \pm 4\text{e}+02$
C1	$1.95\text{e}+05 \pm 7\text{e}+03$	$9.98\text{e}+04 \pm 7\text{e}+03$	$3.33\text{e}+04 \pm 8\text{e}+02$
C2	$3.07\text{e}+05 \pm 6\text{e}+03$	$6.27\text{e}+04 \pm 4\text{e}+03$	$680 \pm 3\text{e}+02$

Table B.5: Electronic noise coefficients from ENC<sup>2</sup> *versus* rise-time curves.

Segment	Feedback R [pA]	$qh_3/A_3$ [pA]
S1	4	93.5
S2	5	997
S3	234	114
S4	2500	2430
S5	100	138
S6	90	291
C1	N/A	3190
C2	N/A	65.1

Table B.6: Leakage current as measured across the feedback resistor with a voltmeter and calculated from the h3 coefficient from the ENC<sup>2</sup> *versus* rise-time curves. The feedback resistor and h3 coefficient measurements were done in October, 2009 and December, 2009 respectively

Detailed measurements with 40  $\mu\text{s}$  traces were conducted in 2009, motivating the reinvestigation of the leakage currents measured in 2003. The 2009

measurements are in qualitative agreement with the 2003 data (S4 dominate source of leakage current) and indicates, for most channels, the parallel noise is roughly consistent with expectations. We do not understand the reason our leakage current increased, or why the values calculated for some channels are inconsistent with the feedback resistor measurements. Because the detector was warmed, pumped, and recooled several times between 2003 and 2009, changes in surface conditions on the contacts may be partially responsible for the observed increase in leakage currents.

### **Appendix C. Resolution**

FWHM values at 1332 keV using both a Gaussian functional fit and a modified Gaussian functional fit [26] are listed in Table C.7. For all but two segments there is at least one channel with a measured value which reaches the targeted resolution goal of 4 keV FWHM at 2039 keV and improvement is expected once several grounding and shielding issues are resolved. It should also be noted that by optimizing the rise-time values for the trapezoidal filter all segments have at least one channel reaching the MAJORANA specification. Also listed are the FWTM/FWHM and FWFM/FWHM ratios for the modified Gaussian functional fit, along with the integrated number of counts in the low-energy tail as a ratio to the number of counts in the photopeak. The deviations from a Gaussian functional fit for the FWFM/FWHM and integrated number of counts in the low-energy tail both suggest charge-collection issues are present for the SXC1 channels.

Segment	FWHM at 1332 keV (Gaussian Fit) [keV]	FWHM at 1332 keV (Modified Gaussian Fit) [keV]	FWTM/FWHM (Modified Gaussian Fit)	FWFM/FWHM (Modified Gaussian Fit)	Low-Energy Tail
C1S1	4.08 ± 0.04	3.98 ± 0.10	1.85 ± 0.06	2.71 ± 0.30	0.021 ± 0.002
C1S2	4.12 ± 0.04	4.04 ± 0.10	1.86 ± 0.07	2.73 ± 0.30	0.007 ± 0.007
C1S3	4.03 ± 0.04	3.96 ± 0.10	1.83 ± 0.05	2.50 ± 0.10	0.009 ± 0.002
C1S4	4.08 ± 0.04	4.04 ± 0.10	1.83 ± 0.05	2.48 ± 0.09	0.019 ± 0.003
C1S5	4.02 ± 0.04	3.96 ± 0.10	1.84 ± 0.05	2.52 ± 0.09	0.010 ± 0.002
C1S6	4.09 ± 0.04	3.93 ± 0.10	1.86 ± 0.07	2.68 ± 0.20	0.013 ± 0.002
C2S1	2.99 ± 0.01	2.96 ± 0.02	1.83 ± 0.01	2.41 ± 0.04	0.007 ± 0.001
C2S2	3.02 ± 0.01	3.00 ± 0.02	1.83 ± 0.02	2.48 ± 0.02	0.023 ± 0.001
C2S3	3.01 ± 0.01	3.01 ± 0.04	1.83 ± 0.03	2.38 ± 0.03	0.006 ± 0.001
C2S4	2.99 ± 0.01	2.99 ± 0.02	1.82 ± 0.01	2.48 ± 0.01	0.019 ± 0.001
C2S5	2.99 ± 0.01	2.98 ± 0.02	1.83 ± 0.02	2.41 ± 0.03	0.005 ± 0.001
C2S6	2.97 ± 0.01	2.95 ± 0.02	1.83 ± 0.01	2.42 ± 0.02	0.007 ± 0.001
S1C1	3.29 ± 0.03	3.13 ± 0.07	1.90 ± 0.05	4.26 ± 0.20	0.064 ± 0.003
S2C1	4.27 ± 0.03	4.10 ± 0.08	1.89 ± 0.05	3.56 ± 0.10	0.042 ± 0.002
S3C1	3.39 ± 0.03	3.32 ± 0.08	1.85 ± 0.05	3.19 ± 0.10	0.028 ± 0.002
S4C1	4.22 ± 0.03	4.13 ± 0.10	1.86 ± 0.05	3.35 ± 0.10	0.038 ± 0.002
S5C1	3.44 ± 0.03	3.33 ± 0.09	1.87 ± 0.06	3.64 ± 0.20	0.043 ± 0.002
S6C1	3.78 ± 0.03	3.63 ± 0.09	1.90 ± 0.05	3.97 ± 0.20	0.049 ± 0.003
S1C2	3.09 ± 0.01	3.06 ± 0.02	1.62 ± 0.20	2.38 ± 0.02	0.005 ± 0.002
S2C2	4.00 ± 0.01	4.00 ± 0.02	1.82 ± 0.01	2.40 ± 0.02	0.002 ± 0.001
S3C2	3.22 ± 0.01	3.21 ± 0.02	1.82 ± 0.01	2.41 ± 0.02	0.002 ± 0.001
S4C2	3.95 ± 0.01	3.99 ± 0.02	1.82 ± 0.01	2.42 ± 0.01	0.004 ± 0.001
S5C2	3.29 ± 0.01	3.28 ± 0.02	1.62 ± 0.20	2.36 ± 0.01	0.002 ± 0.001
S6C2	3.62 ± 0.01	3.53 ± 0.10	1.85 ± 0.08	2.41 ± 0.10	0.002 ± 0.002

Table C.7: FWHM values for each physical segment at 1332 keV from the Gaussian functional fits and modified Gaussian functional fits. Also listed are the FWTM/FWHM and FWFM/FWHM ratios for the modified Gaussian functional fits, along with the integrated number of counts in the low-energy tail as a ratio to the number of counts in the photopeak.

## References

- [1] C. E. Aalseth et al., Phys. Atom. Nucl., vol. 67, (2004), 2002
- [2] A. G. Schubert et al., AIP Conf. Proc. 1441, (2012), 480
- [3] J. F. Wilkerson et al., J. Phys. Conf. Ser. 375 042010, (2012)
- [4] L. Camilleri, E. Lisi, J.F. Wilkerson, Annu. Rev. Nucl. Part. Sci., vol. 58, (2008), 343
- [5] F. T. Avignone III, S. R. Elliott, and J. Engel, Rev. Mod. Phys., vol. 80, (2008), 481
- [6] A. S. Barabash, Phys. Atom. Nucl., vol. 73, (2010), 162

- [7] P. S. Barbeau, J. I. Collar, and O. Tench, *J. of Cosmol. and Astropart. Phys.*, vol. 9, (2007)
- [8] D. G. Phillips II et al., *J. Phys. Conf. Ser.* 381 012044, (2012)
- [9] S. R. Elliott et al., *Nucl. Instr. and Meth.* A558, (2006), 504
- [10] M.A. Deleplanque et al., *Nucl. Instr. and Meth.* A430, (1999), 292
- [11] I. Abt et al., *Nucl. Instr. and Meth.* A570, (2007), 479
- [12] A. R. Young et al, Internal MAJORANA document, (2007), Full publication of these results is in development
- [13] M. Descovich et al., *Nucl. Instr. and Meth.* A553, (2005), 535
- [14] F. Recchia et al., *Nucl. Instr. and Meth.* A604, (2009), 555
- [15] I. Abt et al., *Nucl. Instr. and Meth.* A577, (2007), 474
- [16] I. Abt et al., JINST 4 P11008, (2009)
- [17] The official ITEP homepage, URL: <http://www.itep.ru>
- [18] The official IGEX homepage, URL: <http://www.nu.to.infn.it>
- [19] The official JINR homepage, URL: <http://www.jinr.ru>
- [20] The official ORTEC homepage, URL: <http://www.ortec-online.com>
- [21] P. Sangsingkeow et al., *Nucl. Instr. and Meth.* A505, (2003), 183. Please contact P. Sangsingkeow (Pat.Sangsingkeow@ametek.com) for more detailed information concerning the PT6x2 geometry.
- [22] J. Eberth et al., *Prog. in Part. and Nucl. Phys.*, vol. 46, (2001), 389
- [23] P. Gamir, Ph. D. Dissertation, Cranfield University, (1997)
- [24] The official Canberra homepage, URL: <http://www.canberra.com>
- [25] The official XIA homepage, URL: <http://www.xia.com>
- [26] K. Debertin and R.G. Helmer,  *$\gamma$  and X-Ray Spectrometry with Semiconductor Detectors*, 1988

- [27] ORTEC, Private Communication
- [28] R. M. Keyser and W. K. Hensley, *IEEE Trans. Nucl. Sci.*, vol. 1, (2002), 275
- [29] B. Bruyneel et al., *Nucl. Instr. and Meth. A*608, (2009), 99
- [30] M. Boswell et al., *IEEE Trans. Nucl. Sci.*, vol. 58, (2011), 1212
- [31] H. Tan et al., *IEEE Trans. Nucl. Sci.*, vol. 51, (2004), 1541
- [32] D. Radford, Private Communication
- [33] G. F. Knoll, *Radiation Detection and Measurement*, Wiley, 1979
- [34] G. Bertuccio and A. Pullia, *Rev. of Sci. Instr.*, vol. 64, (2009), 3294
- [35] E. Gatti et al., *Nucl. Instr. and Meth. A*297, (1990), 467
- [36] W. E. Drummond, *IEEE Trans. Nucl. Sci.*, vol. NS18, (1971), 91
- [37] H. V. Klapdor-Kleingrothaus, *Eur. Phys. A* 12, (2001), 148
- [38] C. E. Aalseth et al., *Phys. Ref. C*, vol. 59, (1999), 2109
- [39] I. Abt et al., *Nucl. Instr. and Meth. A*583, (2007), 332
- [40] V. E. Guiseppe et al., *IEEE Nucl. Sci. Symp. Conf. Rec.*, (2008), 1793